Tunable hybridized plasmons–phonons in a graphene/mica-nanofilm heterostructure†

Yaling Qin,‡[a,b] Min Liu,‡[a,b] Hanchao Teng,[b,c] Na Chen,[b,c] Chenchen Wu,[b,c] Chengyu Jiang,[b,c] Zhuoxin Xue,[b,c] Hualong Zhu,[b,c] Jiayi Gui,[b,c] Xiang Liu,*[d] Yuchuan Xiao*[b,c] and Hai Hu *[b,c]

Graphene plasmons exhibit significant potential across diverse fields, including optoelectronics, metamaterials, and biosensing. However, the exposure of all surface atoms in graphene makes it susceptible to surrounding interference, including losses stemming from charged impurity scattering, the dielectric environment, and the substrate roughness. Thus, designing a dielectric environment with a long lifetime and tunability is essential. In this study, we created a van der Waals (vdW) heterostructure with graphene nanoribbons and mica nano-films. Through Fourier-transform infrared spectroscopy, we identified hybrid modes resulting from the interaction between graphene plasmons and mica phonons. By doping and manipulating the structure of graphene, we achieved control over the phonon–plasmon ratio, thereby influencing the characteristics of these modes. Phonon-dominated modes exhibited stable resonant frequencies, whereas plasmon-dominated modes demonstrated continuous tuning from 1140 to 1360 cm^{-1} in resonance frequency, accompanied by an increase in extinction intensity from 0.1% to 1.2%. Multiple phonon couplings limited frequency modulation, yielding stable resonances unaffected by the gate voltage. Mica substrates offer atomic level flatness, long phonon lifetimes, and dielectric functionality, enabling hybrid modes with high confinement, extended lifetimes (up to 1.9 picoseconds), and a broad frequency range (from 750 cm^{-1} to 1450 cm^{-1}). These properties make our graphene and mica heterostructure promising for applications in chemical sensing and integrated photonic devices.

Introduction

Plasmons, quasi-particles resulting from the coupling of incident light with free electrons in a conductor, are pivotal in transforming three-dimensional free-space light into specialized lower-dimensional interface electromagnetic waves. This transformation leads to efficient wavelength confinement and significant field enhancement effects. Compared to traditional noble metals such as gold and silver,[1,2] two-dimensional materials like graphene exhibit unique advantages including atomic-level thickness, distinct band structures, ultra-high carrier mobility, and tunable carrier concentration *via* gate voltage.[3–9] Consequently, the plasmons supported by graphene demonstrate extreme optical field confinement,[10–12] a broad range of spectral response frequencies,[13–15] ultra-long transmission lifetimes,[16–19] and dynamic control capabilities.[20–24] These properties make them suitable for a wide array of applications, spanning fields from physics and information science to chemistry.[25–27] Notable applications include enhanced vibrational spectroscopy techniques like surface-enhanced infrared absorption spectroscopy[28–32] and surface-enhanced Raman spectroscopy[33] in sensor technologies,[34] on-chip active devices such as tunable single-photon sources[35] and lasers,[36] and various passive components including waveguides, modulators, switches, and detectors.[37–42]

However, the structural properties of graphene as a two-dimensional material present both advantages and challenges for surface plasmons. While its single-atom thickness provides a highly confined platform, it also makes the material highly susceptible to interference from the surrounding dielectric environment.[17,18,43] This vulnerability manifests as multiple loss mechanisms, including charged impurity scattering, acoustic phonon scattering, electron–electron scattering, and

[a]*School of Materials Science and Engineering, Henan Institute of Advanced Technology, Zhengzhou University, Zhengzhou, 450001, China*
[b]*CAS Key Laboratory of Nanophotonic Materials and Devices, CAS Key Laboratory of Standardization and Measurement for Nanotechnology, National Center for Nanoscience and Technology, Beijing 100190, P. R. China. E-mail: huh@nanoctr.cn, xiaoyc@nanoctr.cn*
[c]*Center of Materials Science and Optoelectronics Engineering, University of Chinese Academy of Sciences, Beijing 100049, P. R. China*
[d]*Nanjing University of Information Science and Technology, Nanjing, 210044 China. E-mail: 002821@nuist.edu.cn*
†Electronic supplementary information (ESI) available. See DOI: **https://doi.org/10.1039/d4nr00942h**
‡These authors contributed equally.

dielectric losses, ultimately limiting the quality factor and propagation distance of graphene plasmons. Consequently, harnessing the full potential of graphene plasmonics hinges on the creation of a tailored dielectric environment that promotes long plasmon lifetimes and tunability.

Significant efforts have been directed towards identifying suitable dielectric substrates for graphene plasmonics. Various high-quality dielectric substrate materials, such as silicon carbide (SiC),[44] silicon dioxide (SiO_2),[45] boron nitride (*h*-BN),[46,47] and suspended structures,[18,48] have been employed as substrates for graphene plasmons in recent years. Among these, we have successfully manufactured flexible graphene plasmon devices using thick mica substrates,[49] showcasing their stability under bending and their highly sensitive performance in surface-enhanced infrared absorption spectroscopy sensing applications.

In this study, we present the design and characterization of a van der Waals heterostructure comprising graphene nanoribbons and mica nano-films. Employing far-field Fourier transform infrared (FTIR) spectroscopy, we unveil the emergence of hybrid modes arising from the interaction between localized graphene plasmons and intrinsic optical phonons within the mica lattice. The coupling of various mica phonons with plasmons leads to a rich tapestry of hybrid modes with distinct characteristics. Notably, we demonstrate the ability to control the relative contributions of phonon and plasmon modes within the hybrid structure by manipulating geometric features and applying the gate voltage. When phonon modes dominate, the resulting hybrid modes exhibit exceptionally long lifetimes and stable resonant frequencies, displaying minimal sensitivity to gate voltage control. Conversely, plasmon-dominated modes exhibit high tunability, showcasing significant shifts in resonant frequencies under gate voltage. Particularly, in cases involving multiple phonon couplings, the proximity of phonon frequencies restricts frequency modulation, resulting in modes with stable resonant frequencies that do not shift spectral lines but exhibit modulation in the extinction intensity by the gate voltage. Our research highlights the advantages of mica substrates, which provide atomic-level flatness, long phonon lifetimes, and advanced dielectric functionality, offering hybrid modes with attributes such as high-wavelength confinement, extended lifetimes, and a broad frequency range. This innovative design offers a new approach to polariton excitation and propagation control at deep subwavelength scales, holding significant promise for the development of novel nanophotonic sensors and circuits.

Methods

Nanofabrication of the devices

Mica nanofilms were mechanically exfoliated from bulk crystals and then transferred onto the silica substrate *via* a deterministic dry transfer process with a PDMS stamp by using a homemade stage under optical microscopy.[50] Due to the nature of this method, the thickness of the obtained nanosheets varied. However, by systematically screening a large number of randomly exfoliated nanosheets on the substrate, we managed to obtain a satisfactory batch with relatively uniform thickness. For device measurements, we used mica nanosheets with a thickness range of 100–300 nm. Graphene sheets were synthesized on copper foil through chemical vapor deposition (CVD) and transferred onto the mica film using a conventional wet technique.[51] Nanoribbon arrays (100 μm × 200 μm) were patterned on the graphene sheet using 100 kV electron-beam lithography (EBL) (Vistec 5000 + ES) on approximately 250 nm of poly (methyl methacrylate) (PMMA 950 K) electron beam lithography resist. The patterns were then etched by oxygen plasma etching at 5 Pa and 75 W for 5 seconds. Then, the sample was immersed in hot butanone at 85 °C for 30 min and subjected to a gentle rinse of IPA for 5 min to remove the resist layer, followed by nitrogen gas drying and thermal baking. Two sets of electrode patterns were defined using another EBL procedure and electron beam evaporation. Electrode patterns were designed on the samples using EBL on approximately 350 nm of PMMA resist. After that, electron-beam evaporation was used to deposit 5 nm Cr and 60 nm Au in a vacuum chamber to fabricate the electrode pads, followed by a lift-off procedure to remove the resist layer.[52]

Mid-infrared microscopy measurements

Infrared transmission measurements were performed using a Fourier Transform Infrared (FTIR) microscope (Thermo Fisher Scientific, Nicolet iN10) equipped with a deuterated L-alanine doped triglycine sulfate (DLATGS) IR detector. The microscope was configured with a high-efficiency 15× objective and condenser, featuring a numerical aperture of 0.7 and an angular range of 40° to 87°. A 100 × 200 μm aperture was employed to obtain the spot size. A spectral resolution of 4 cm^{-1} was used for all spectra. Single-beam transmittance spectra were collected at the charge neutral point as a reference to calculate the extinction spectra of the various doped graphene nanoribbons (ESI Fig. 1†). All measurements were conducted at ambient temperature and under standard atmospheric conditions.

Results and discussion

To efficiently hybridize plasmon and phonon modes in graphene/mica heterostructures, we engineered a graphene nanoribbon array on a mica substrate (Fig. 1a–c). The mica substrate, approximately 280 nm thick, was mechanically exfoliated and transferred onto a silicon substrate. This was followed by the wet transfer of large-area graphene onto the substrate to cover the mica film. Subsequently, the graphene was structured into electrically continuous nanoribbon arrays, and Cr/Au electrodes were applied to facilitate electrical adjustment of the doping levels of the graphene nanoribbons (see the Methods section for details of the sample fabrication). We further employed atomic force microscopy (AFM) to analyse the morphology of the fabricated graphene nanoribbons, con-

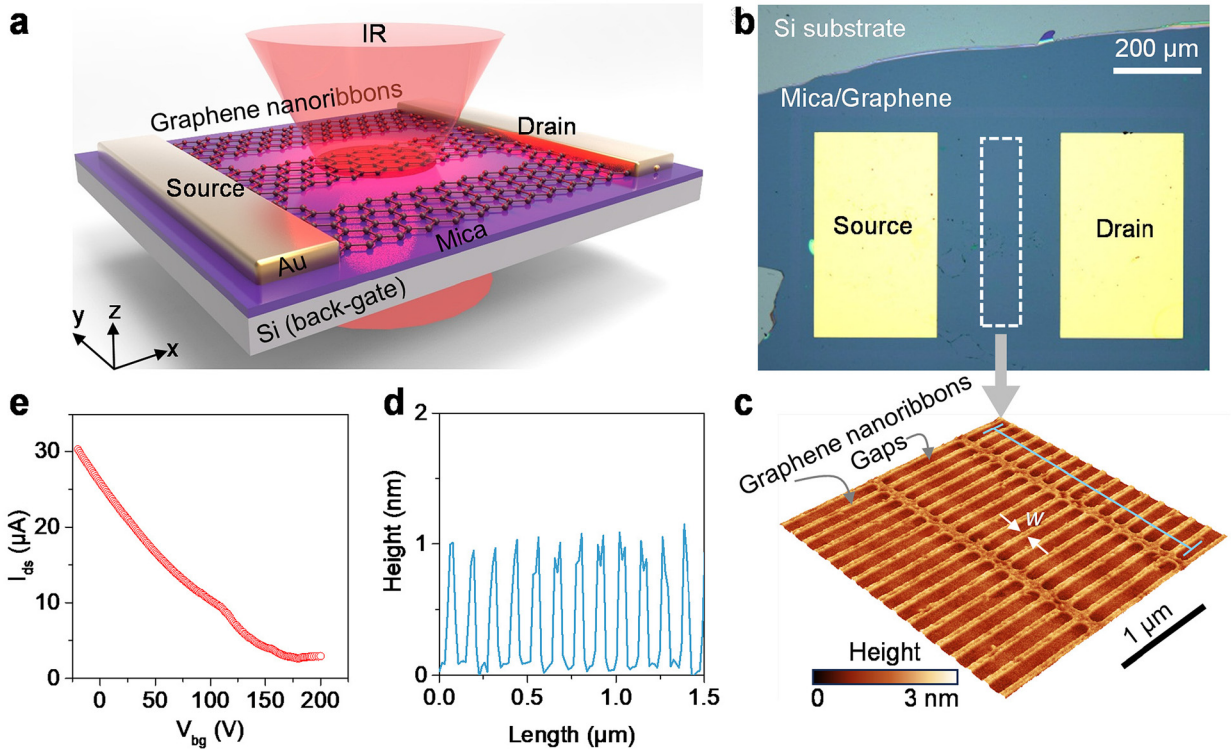

Fig. 1 Experimental setup. (a) Schematic diagram illustrating the sample structure and measurement method. Graphene nanoribbons are integrated with nanometer-thick mica films to create a vdW heterostructure. This structure is placed on a silicon substrate with metal electrodes positioned on top. The extinction signal of the device is collected using Fourier infrared spectroscopy. (b) Optical image of the sample. The highlighted area enclosed by the white dashed box denotes the region of graphene nanoribbons. The mica thickness measures ~280 nm, with the scale bar indicating 200 μm. (c) Topography of graphene nanoribbons. The ratio of the prepared ribbons to the gaps is approximately 1 : 1.5. Notably, large periodic ribbons are apparent along the *y*-axis, providing support for the nanoribbons during preparation and ensuring electrical continuity in measurement. The scale bar corresponds to 1 μm. (d) Height profile of graphene nanoribbons, extracted from the white line in panel (c). (e) Transfer curve of the device. During testing, the silicon substrate functions as the back gate, the mica layer acts as an effective dielectric layer, while the graphene monolayer and the areas designated as nanoribbons collectively form the channel.

firming their size and uniformity, and evaluating impurities introduced during fabrication. As shown in Fig. 1c and d, the width of the fabricated ribbons is approximately 65 nm, with a gap width of around 100 nm. Moreover, both the overall uniformity of the ribbons and the cleanliness of the sample surface demonstrate high quality (ESI Fig. 2†).

Furthermore, electrical property testing was carried out on the device. Analysis of Fig. 1e reveals a gradual decrease in channel current with increasing gate voltage, eventually stabilizing at a minimum, with which the gate voltage hits ~200 V. This trend underscores the efficient dielectric properties of the mica film as an insulating layer, facilitating effective electron injection doping into graphene. Additionally, the Dirac point shifts towards such high positive voltages, indicating that our prepared sample manifests significant intrinsic p-type doping effects. This behaviour can be attributed to two primary factors: charge transfer doping of graphene by solvents during the fabrication process[53] and charge-induced doping of graphene by dangling chemical bonds on the mica surface.[54,55] Through these electrical measurements, we have pinpointed the gate voltage of 200 V as the charge neutral point (CNP), where the graphene doping concentration approaches E_F = 0 eV. The CNP facilitates the next step of *in situ* spectroscopic measurements.

Upon characterizing the basic properties of the device, we have formally initiated an exploration of the plasmonic response of the device. We primarily employed a Fourier transform infrared spectrometer to investigate the extinction characteristics of graphene nanoribbon regions. Initially, the graphene doping was tuned to approximately zero (*i.e.*, near the CNP), and a single-beam transmittance spectrum, T_{CNP}, was recorded as the background signal. Subsequently, the gate voltage was varied to gradually increase the doping concentration of graphene, and single-beam transmittance spectra, T_{gate}, were consecutively measured for different doping levels. The resulting extinction spectrum was then calculated using the formula $T = 1 - T_{gate}/T_{CNP}$ (for details on spectrum measurement, refer to the Methods section).

Fig. 2a illustrates the modulation of the extinction spectrum of a graphene nanoribbon array with a width of 65 nm (corresponding to the sample in Fig. 1) in response to changes in gate voltages. It is evident that as the gate voltage is decreased gradually, indicating an increase in graphene nanoribbon doping, the overall peak positions of the extinction

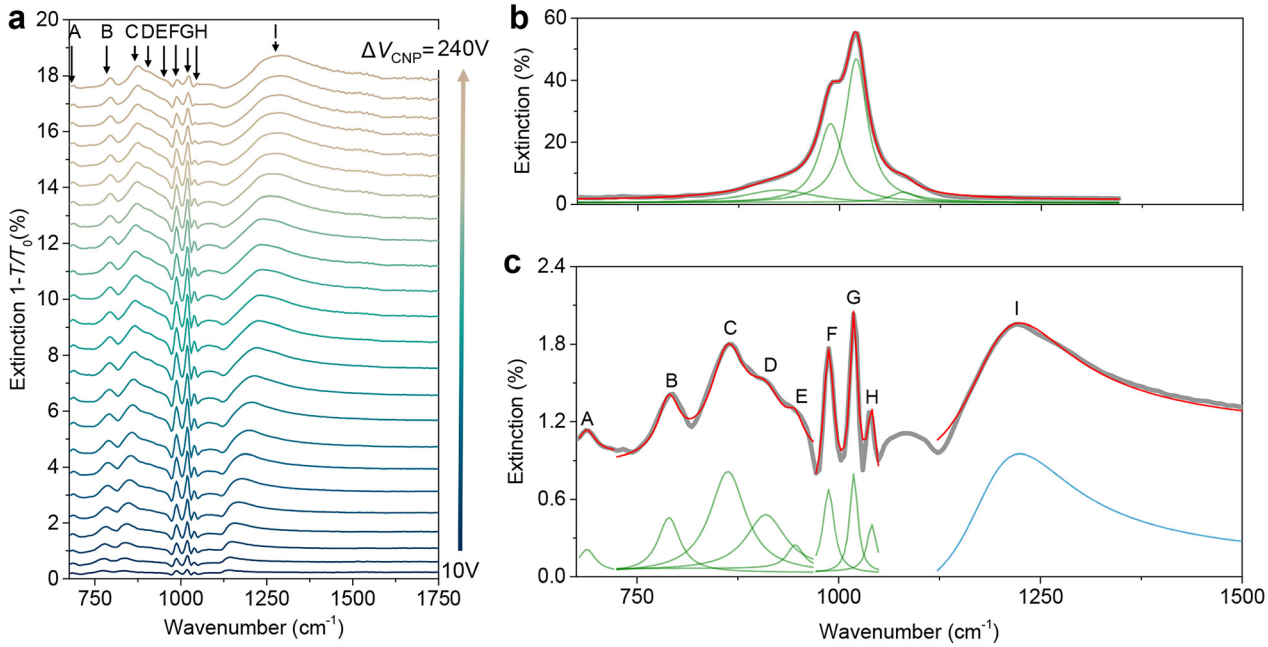

Fig. 2 Spectral collection and fitting. (a) Extinction spectra of graphene nanoribbon regions under different gate voltages. The voltage difference (ΔV_{CNP}) between the applied gate voltage and the CNP increases from 10 V to 240 V. Peaks in the curve are labeled with letters A–I. (b) Measured infrared absorption spectrum of the mica nanofilm in the device (gray curve). The red curve represents the fitted curve, and the green curve represents the constituent sub-peaks of the fitted curve. (c) Fitting and analysis of the extinction spectra of hybridized modes in graphene and mica vdW heterostructures. The gray lines represent the experimentally collected original signals. The red line represents the fitted curve. The A–H peaks are from Lorentzian fitting (green), and the I peak is from Fano fitting (blue).

spectrum shift towards higher frequencies, accompanied by a significant variation in extinction intensity. The resulting extinction spectrum forms a complex curve with nine distinct peaks, differing significantly from that on a SiO_2 substrate (ESI Fig. 3†), each sequentially labelled as A–I. In ESI Fig. 4,† we fabricated another device with a ribbon width of ~60 nm and performed spectral measurements. Both devices exhibit well-defined spectral peaks, demonstrating excellent reproducibility. Notably, in Fig. 2a, peaks A–H display a progressive blue shift in position with decreasing voltage, showing an initial increase in intensity followed by a decrease, whereas the intensity and position of peak I exhibit a consistent increase.

To further investigate the origins of these multiple peaks, we conducted additional testing on the extinction spectrum of the mica region not covered by graphene, as illustrated in Fig. 2b. The complex band (~1100 cm^{-1}) is assigned to stretching Si–O–Si vibrations.[56] The absorption of these phonon modes overlaps with the resonance frequency of intrinsic graphene plasmons. It is noteworthy that the peaks of mica at this frequency result from the contributions of multiple phonons,[56] as evidenced by Lorentzian fitting, and coincided with previous studies.[57] Thus, the complex extinction spectrum observed is a consequence of the interaction between the localized plasmons of graphene nanoribbons and the multiple phonons of the mica nanofilm.

To further analyse the properties of these modes, we extracted their peak frequency (Fig. 3a), extinction intensities (Fig. 3b), and FWHM (Fig. 3c). Through the extracted data analysis, the A–I peaks can be roughly classified into three categories. The first type consists of peaks with resonance frequencies far from mica phonons, where the components of graphene plasmons dominate, such as peak I. Their origins resemble the Fano effect, where graphene plasmons act as a broad continuous spectrum, while the phonon peaks represent a narrow discrete spectrum within it. The second scenario involves hybrid modes formed when plasmons and phonon peaks are nearby. In such cases, due to the proximity in frequencies, a phenomenon similar to plasmon-induced transparency (PIT).[58] PIT can also be seen as a special case of Fano resonance, characterized by a symmetric Lorentzian-shaped peak (*e.g.*, peaks FGH). In Fig. 2c, we demonstrate the results of fitting these complex peak shapes using Lorentzian (peaks FGH) and Fano models (peak I). Our experimental curves in grey align closely with the red fitting curves. The third type of peak is mainly situated between these two, such as (peaks A–E), where their spectra are not entirely symmetrical, but the degree of asymmetry in the rise and fall of the peaks does not match typical Fano peaks. In practical fitting, these peaks are closer to Lorentzian peaks.

The I peak is flexibly controlled by gate voltage. Its resonance peak can be continuously tuned from 1150 cm^{-1} to 1300 cm^{-1}. In another sample we prepared, a broader electrical modulation range was achieved, enabling continuous tuning from 1140 cm^{-1} to 1360 cm^{-1} (ESI Fig. 4†). In contrast, the

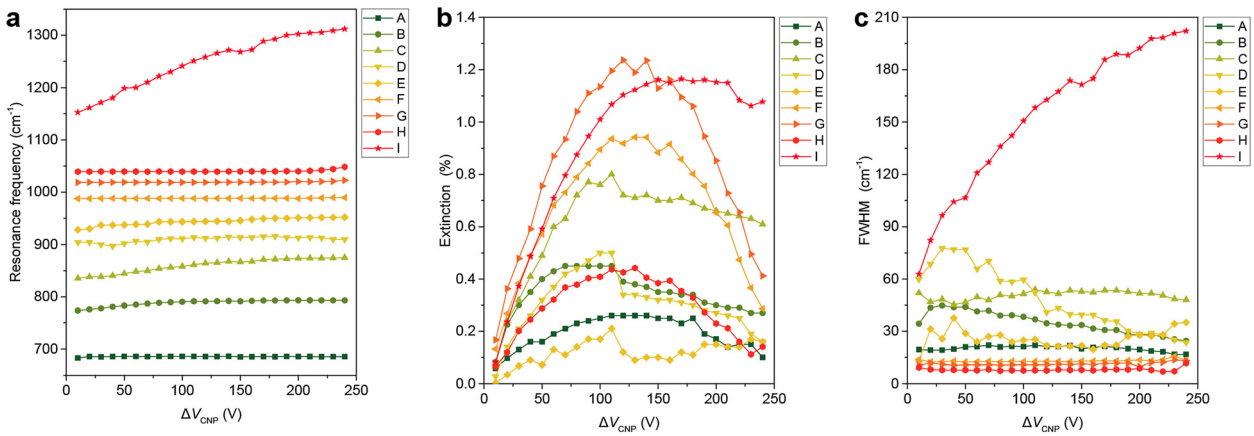

Fig. 3 Extinction spectrum analysis. Relationship between the resonance frequencies (a), extinction intensities (b), and the full width at half maximum (FWHM) (c) of peaks A–I and voltage difference ΔV_{CNP}.

positions of peaks A, F, G, and H show little variation. Particularly for the F and G modes, their peaks are sandwiched between other phonon modes, resulting in minimal resonance frequency shifts. The remaining peaks whose resonant frequencies can be slightly changed, for example, peak B can be modulated from 750 cm^{-1} to 790 cm^{-1}. By observing the degree to which these peaks can be modulated, we can also roughly distinguish that the I peak is predominantly influenced by plasmon components, while the A, F, G, and H phonon modes dominate. The other peaks, B, C, D, and E, exhibit a more balanced distribution of the two components.

Compared to resonance frequencies, gate voltage tunability has a more significant impact on the intensity of all the peaks. As shown in Fig. 3b, with increasing doping, the intensity of the I peak gradually rises, with the extinction intensity increasing from 0.1% to 1.2%. The modulation of the other peaks is not a simple monotonic increase and the intensity first increases and then decreases. This is because the extinction intensity is constrained by a trade-off of resonance frequencies and doping concentration. The initial increase in extinction intensity occurs due to carrier injection enhancing the absorption of plasmon modes, while the subsequent decrease is attributed to the resonance frequency of graphene plasmons moving away from the frequency positions of these hybrid modes.

The modulation of FWHM follows a similar trend to extinction intensity. With increasing doping, the FWHM of the I peak gradually increases. This is attributed to the influence of plasmons in the modes, where higher doping levels amplify electron–phonon scattering and electron–electron scattering, leading to a decrease in the lifetime of plasmons. This pattern aligns with observations in SiO_2 dielectric substrates (ESI Fig. 3†). Additionally, it can be observed that the widths of hybrid modes are exceptionally narrow, particularly for the F and G peaks that are dominated by phonon modes, with widths of only over ten wavenumbers. To the best of our knowledge, this may represent the narrowest width observed for plasmons in the mid-infrared range.[5]

Mica is widely recognized for its atomically flat surface,[59] which is expected to help reduce interface scattering and enhance the lifetime of graphene plasmons. Additionally, the long-lived phonons in mica can further contribute to extending the lifetime of hybrid modes. Therefore, for a more thorough quantitative analysis of the ability of mica substrate to enhance the lifetime of graphene plasmons, we further prepared substrates of regular SiO_2 and mica/SiO_2 (as shown in Fig. 4a). On these two substrates, nanoribbons of different widths were prepared (ESI Fig. 5†), corresponding to different graphene plasmon wavevectors, and extinction spectra were conducted under the same ribbon width and doping concentration (as shown in Fig. 4b). As the strip width decreases, the wave vector of the hybrid plasmon increases, leading to a significant blue shift of its resonance frequency from 750 cm^{-1} to 1450 cm^{-1} on the mica substrate.

Similar to the previous description, we can classify the first two peaks as plasmon-phonon hybrid modes, while identifying the last major peak as a plasmon mode. It is evident that as the ribbon width decreases, corresponding to an increase in wave vector, the resonance frequency of graphene plasmons shifts towards the blue end of the spectrum range. The mica thickness used in our experiments is only ~100 nm, which is one-third of the thickness of the SiO_2 substrate. Consequently, the spectra on this mica/SiO_2 substrate exhibit a significantly different shape compared to those in Fig. 2, with the overall spectral profile here bearing a closer resemblance to that of the SiO_2 substrate.

A comparison indicates that at different ribbon widths, the spectra on the mica substrate exhibit a redshift towards lower frequencies compared to those on the SiO_2 substrate. Additionally, in contrast to the plasmon modes, the FWHM of the plasmon mode at each width is narrower. Through quantitative analysis, we further extracted lifetimes as depicted in Fig. 4c, revealing that the overall lifetimes on the mica substrate are higher than those on the SiO_2 substrate. At a ribbon width of 180 nm, the plasmon lifetimes on both substrates reach the maximum value, with the plasmon lifetime on the

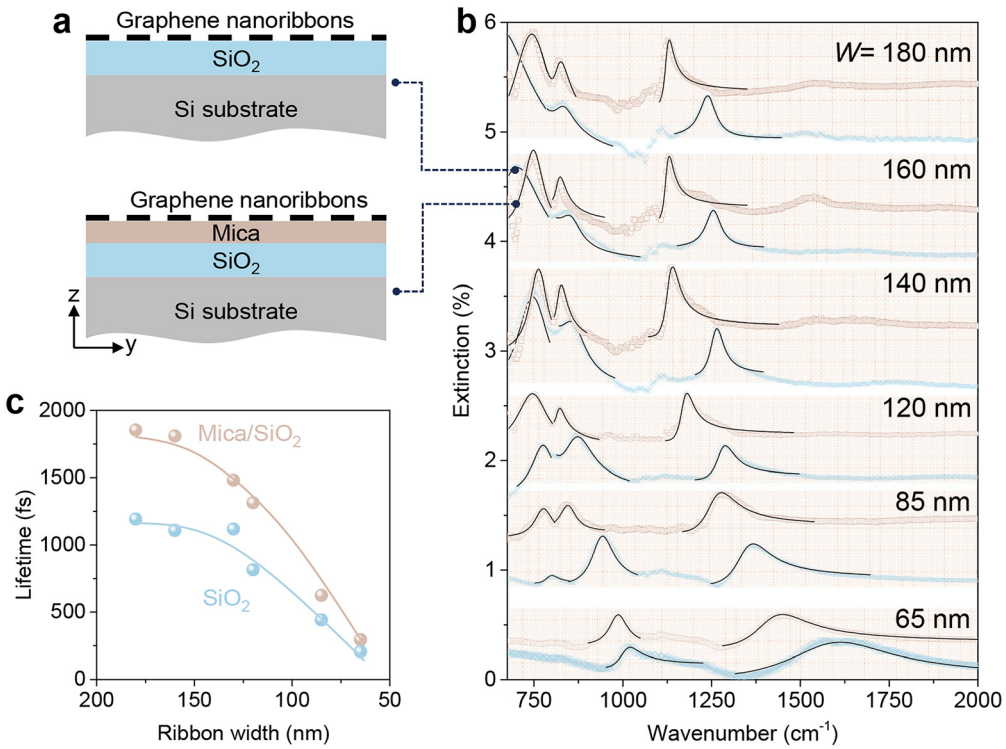

Fig. 4 Analysis of lifetime. (a) Schematic cross-section of device structures. The lower part shows a device with silicon dioxide covered by mica. The upper part depicts a conventional device on a silicon dioxide substrate, serving as a control experiment. (b) Extinction spectra with different widths of graphene nanoribbons. The blue curves correspond to the extinction spectra of samples on a silicon dioxide substrate, while the brown curves correspond to those of a mica/silicon dioxide substrate. The light background represents a set of contrast experiments with the same widths and doping concentrations of graphene nanoribbons. (c) Relationship between hybrid mode lifetime and the width of graphene nanoribbons.

mica substrate being approximately 1.9 picoseconds, compared to around 1.0 picoseconds on the SiO_2 substrate. This experiment conclusively demonstrates that the mica substrate serves as a crucial platform for graphene plasmons with enhanced quality factors.

It should be noted here that the difference in dielectric function between mica and silicon oxide will also affect the resonant frequency and lifetime of graphene plasmons. A higher dielectric constant leads to a redshift in the resonant frequency. As the dielectric constant increases, the restoring force acting on the oscillating charge density of the plasmon also strengthens, resulting in a lower resonant frequency. The lifetime of graphene plasmons is another critical parameter that is influenced by the dielectric constant. The plasmonic quality factor (Q) can be decomposed into two additive components:[17] an intrinsic component and an environmental component, $Q^{-1} = \frac{q_p''}{q_p'} \approx \frac{\sigma'}{\sigma''} + \frac{\kappa''}{\kappa'}$, where q_p' and q_p'' are the real and imaginary parts of the complex momentum of graphene plasmons, respectively. σ and κ are the optical conductivity of graphene and effective permittivity. The lifetime can be obtained using $\tau = 2\frac{q_p'}{\omega q_p''}$, where ω is the frequency. The inherent component originates from scattering events occurring within the graphene layer, whereas the extrinsic component results from energy dissipation to the adjacent dielectric medium. To determine the extent of these dielectric losses, we require the effective permittivity, which is given by $\kappa = \kappa'(q,\omega) + \kappa''(q,\omega)$. The effective dielectric constant considers the contribution of the dielectrics above and below the graphene. At frequencies exceeding 1580 cm^{-1}, graphene plasmons can decay by the intraband Landau damping regime, in which the plasmon damping process is mediated by the emission of an optical phonon. This coupling between the plasmon and the optical phonon lattice vibrations leads to the generation of electron–hole pairs and a consequent decrease in the plasmon lifetime.[43]

We have further identified the phenomenon of graphene plasmons simultaneously coupling with mica phonons and SiO_2 phonons. As illustrated in ESI Fig. 6,† despite the peak splitting caused by the silicon dioxide phonon at ~1168 cm^{-1}, we are still able to observe the narrow peak of plasmon coupling with mica phonons. This trilateral coupling phenomenon in the graphene plasmon system is of paramount significance for the applications of molecular enhancement, as it establishes a crucial groundwork for analysing mixtures such as the products of catalytic reactions and complex bacteria and viruses in tears where the absorption peaks of molecules overlap.[60] Our highly efficient, electrically regulated graphene plasmons also have the potential to couple with in-plane

bending hyperbolic phonon polaritons, advancing the development of Mach–Zehnder electro-optic modulators.[51,61]

We determined the dielectric function of mica by Lorentz fitting its absorption spectrum and used this function in COMSOL Multiphysics simulations to model the extinction spectra from the coupling between graphene plasmons and mica (ESI Note 1†). The discrepancies between our theoretical and experimental results can be attributed to the complex phonon modes of mica, which become more intricate when coupled with graphene plasmons. Notably, we have not yet fully resolved all the phonon modes of mica, especially the longitudinal ones, which are perpendicular to the far-field direction and challenging to detect directly. These phonons couple with graphene plasmons, resulting in complex peaks in the Fourier transform infrared spectrum.

Conclusions

We have engineered a van der Waals heterostructure consisting of graphene nanoribbons and nanometer-thick mica films and identified hybrid modes of coupling between localized graphene plasmons and mica optical phonons using far-field Fourier infrared spectroscopy. The coupling of multiple optical phonons in mica with plasmons has given rise to a variety of hybrid modes with distinct characteristics. By manipulating the gate voltage doping and varying geometric structures, we have managed to regulate the proportion of phonon modes and plasmon modes within the hybrid modes. In scenarios where phonons are predominant, the modes exhibit prolonged lifetimes and stable resonance frequencies that are less responsive to gate voltage adjustments. Conversely, when plasmons take the lead, the modes become more tunable, allowing for significant alterations in resonance frequencies. In situations involving multiple phonon couplings, the modulation capabilities of phonons in close proximity restrict frequency shifts, leading to modes where resonance frequencies remain unchanged, resulting in unique modes only with the extinction intensity controlled by the gate voltage. Our study demonstrates that mica substrates offer precise atomic-level flatness, extended phonon lifetimes, and superior dielectric properties, enabling hybrid modes with attributes such as highly confined wavelengths, enduring lifespans, and broad frequency ranges. These characteristics present promising prospects for applications like chemical sensing and integrated photonic devices.

Author contributions

H. H., X. L., and Y. X. conceived the study. M. L. and Y. Q. led the experimental work, including sample preparation and mid-infrared microscopy measurements. H. T., N. C., C. W., C. J., Z. X., H. Z., and J. G. developed the data fitting algorithm and COMSOL Multiphysics simulations and provided experimental assistance. All authors contributed to data analysis, interpretation of results, and manuscript discussions. Y. Q. and M. L. jointly wrote the manuscript, incorporating feedback and suggestions from all contributors.

Data availability

The data that support the findings of this study are all available and archived in the manuscript and the ESI.†

Conflicts of interest

There are no conflicts to declare.

Acknowledgements

The National Natural Science Foundation of China grants 52322209, 52172139, 52350314; This work was funded in part by the National Key Research and Development Program of China grants 2021YFA1201500 and 2020YFB2205701, the Beijing Nova Program grants 2022012 and 20240484600, the Youth Innovation Promotion Association of the Chinese Academy of Sciences grant 2022037, and the Strategic Priority Research Program of the Chinese Academy of Sciences grant XDB36000000.

References

1 A. Boltasseva and H. Atwater, Low-loss plasmonic metamaterials, *Science*, 2011, **331**, 290–291, DOI: **10.1126/science.1198258**.

2 P. R. West, S. Ishii, G. V. Naik, N. K. Emani, V. M. Shalaev and A. Boltasseva, Searching for better plasmonic materials, *Laser & Photonics Rev.*, 2010, **4**, 795–808, DOI: **10.1002/lpor.200900055**.

3 A. N. Grigorenko, M. Polini and K. Novoselov, Graphene plasmonics, *Nat. Photonics*, 2012, **6**, 749–758, DOI: **10.1038/nphoton.2012.262**.

4 F. Javier García de Abajo, Graphene plasmonics: challenges and opportunities, *ACS Photonics*, 2014, **1**, 135–152, DOI: **10.1021/ph400147y**.

5 S. Huang, C. Song, G. Zhang and H. Yan, Graphene plasmonics: physics and potential applications, *Nanophotonics*, 2016, **6**, 1191–1204, DOI: **10.1515/nanoph-2016-0126**.

6 A. K. Geim, Graphene: status and prospects, *Science*, 2009, **324**, 1530–1534, DOI: **10.1126/science.1158877**.

7 S. Han, S. Kim, S. Kim, T. Low, V. W. Brar and M. S. Jang, Complete Complex Amplitude Modulation with Electronically Tunable Graphene Plasmonic Metamolecules, *ACS Nano*, 2020, **14**, 1166–1175, DOI: **10.1021/acsnano.9b09277**.

8 Y. Dong, L. Xiong, I. Y. Phinney, Z. Sun, R. Jing, A. S. McLeod, S. Zhang, S. Liu, F. L. Ruta, H. Gao, Z. Dong, R. Pan, J. H. Edgar, P. Jarillo-Herrero, L. S. Levitov, A. J. Millis, M. M. Fogler, D. A. Bandurin and D. N. Basov,

Fizeau drag in graphene plasmonics, *Nature*, 2021, **594**, 513–516, DOI: **10.1038/s41586-021-03640-x**.

9 W. Zhao, S. Zhao, H. Li, S. Wang, S. Wang, M. I. B. Utama, S. Kahn, Y. Jiang, X. Xiao, S. Yoo, K. Watanabe, T. Taniguchi, A. Zettl and F. Wang, Efficient Fizeau drag from Dirac electrons in monolayer graphene, *Nature*, 2021, **594**, 517–521, DOI: **10.1038/s41586-021-03574-4**.

10 I. David Alcaraz, S. Nanot, E. J. Dias, I. Epstein, C. Peng, D. K. Efetov, M. B. Lundeberg, R. Parret, J. Osmond and J. Hong, Probing the ultimate plasmon confinement limits with a van der Waals heterostructure, *Science*, 2018, **360**, 291–295, DOI: **10.1126/science.aar8438**.

11 V. W. Brar, M. S. Jang, M. Sherrott, J. Lopez and H. Atwater, Highly confined tunable mid-infrared plasmonics in graphene nanoresonators, *Nano Lett.*, 2013, **13**, 2541–2547, DOI: **10.1021/nl400601c**.

12 I. Epstein, D. Alcaraz, Z. Huang, V. Pusapati, J.-P. Hugonin, A. Kumar, X. M. Deputy, T. Khodkov, T. G. Rappoport, J.-Y. Hong, N. M. R. Peres, J. Kong, D. R. Smith and F. Koppens, Far-field excitation of single graphene plasmon cavities with ultra compressed mode volumes, *Science*, 2020, **368**, 1219–1223, DOI: **10.1126/science.abb1570**.

13 T. Low and P. Avouris, Graphene plasmonics for terahertz to mid-infrared applications, *ACS Nano*, 2014, **8**, 1086–1101, DOI: **10.1021/nn406627u**.

14 L. Ju, B. Geng, J. Horng, C. Girit, M. Martin, Z. Hao, H. A. Bechtel, X. Liang, A. Zettl and Y. Shen, Graphene plasmonics for tunable terahertz metamaterials, *Nat. Nanotechnol.*, 2011, **6**, 630–634, DOI: **10.1038/nnano.2011.146**.

15 M. S. Ukhtary and R. Saito, Surface plasmons in graphene and carbon nanotubes, *Carbon*, 2020, **167**, 455–474, DOI: **10.1016/j.carbon.2020.05.019**.

16 A. Woessner, M. B. Lundeberg, Y. Gao, A. Principi, P. Alonso-González, M. Carrega, K. Watanabe, T. Taniguchi, G. Vignale and M. Polini, Highly confined low-loss plasmons in graphene–boron nitride heterostructures, *Nat. Mater.*, 2015, **14**, 421–425, DOI: **10.1038/nmat4169**.

17 G. Ni, d. A. McLeod, Z. Sun, L. Wang, L. Xiong, K. Post, S. Sunku, B.-Y. Jiang, J. Hone and C. Dean, Fundamental limits to graphene plasmonics, *Nature*, 2018, **557**, 530–533, DOI: **10.1038/s41586-018-0136-9**.

18 H. Hu, R. Yu, H. Teng, D. Hu, N. Chen, Y. Qu, X. Yang, X. Chen, A. McLeod and P. Alonso-González, Active control of micrometer plasmon propagation in suspended graphene, *Nat. Commun.*, 2022, **13**, 1465, DOI: **10.1038/s41467-022-28786-8**.

19 L. Kim, S. Kim, P. K. Jha, V. W. Brar and H. Atwater, Mid-infrared radiative emission from bright hot plasmons in graphene, *Nat. Mater.*, 2021, **20**, 805–811, DOI: **10.1038/s41563-021-00935-2**.

20 H. Hu, F. Zhai, D. Hu, Z. Li, B. Bai, X. Yang and Q. Dai, Broadly tunable graphene plasmons using an ion-gel top gate with a low control voltage, *Nanoscale*, 2015, **7**, 19493–19500, DOI: **10.1039/C5NR05175D**.

21 A. Woessner, Y. Gao, I. Torre, M. B. Lundeberg, C. Tan, K. Watanabe, T. Taniguchi, R. Hillenbrand, J. Hone and M. Polini, Electrical 2π phase control of infrared light in a 350 nm footprint using graphene plasmons, *Nat. Photonics*, 2017, **11**, 421–424, DOI: **10.1038/nphoton.2017.98**.

22 H. Hu, N. Chen, H. Teng, R. Yu, M. Xue, K. Chen, Y. Xiao, Y. Qu, D. Hu, J. Chen, P. Li, F. Javier García de Abajo and Q. Dai, Gate-tunable negative refraction of mid-infrared polaritons, *Science*, 2023, **379**, 558–561, DOI: **10.1126/science.adf1251**.

23 T. Huang, X. Tu, C. Shen, B. Zheng, J. Wang, H. Wang, K. Khaliji, S. H. Park, Z. Liu, T. Yang, Z. Zhang, L. Shao, X. Li, T. Low, Y. Shi and X. Wang, Observation of chiral and slow plasmons in twisted bilayer graphene, *Nature*, 2022, **605**, 63–68, DOI: **10.1038/s41586-022-04520-8**.

24 P. Gonçalves, T. Christensen, N. Peres, A. Jauho, I. Epstein, F. Koppens, M. Soljačić and N. Mortensen, Quantum surface-response of metals revealed by acoustic graphene plasmons, *Nat. Commun.*, 2021, **12**, 3271, DOI: **10.1038/s41467-021-23061-8**.

25 L. Cui, J. Wang and M. Sun, Graphene plasmon for optoelectronics, *Rev. Phys.*, 2021, **6**, 100054, DOI: **10.1016/j.revip.2021.100054**.

26 Y. Fan, N. Shen, F. Zhang, Q. Zhao, H. Wu, Q. Fu, Z. Wei, H. Li and C. Soukoulis, Graphene Plasmonics: A Platform for 2D Optics, *Adv. Opt. Mater.*, 2019, **7**, 1800537, DOI: **10.1002/adom.201800537**.

27 K. Yoshioka, G. Bernard, T. Wakamura, M. Hashisaka, K.-i. Sasaki, S. Sasaki, K. Watanabe, T. Taniguchi and N. Kumada, On-chip transfer of ultrashort graphene plasmon wave packets using terahertz electronics, *Nat. Electron.*, 2024, **7**, 537–544, DOI: **10.1038/s41928-024-01197-x**.

28 H. Hu, X. Yang, F. Zhai, D. Hu, R. Liu, K. Liu, Z. Sun and Q. Dai, Far-field nanoscale infrared spectroscopy of vibrational fingerprints of molecules with graphene plasmons, *Nat. Commun.*, 2016, **7**, 12334, DOI: **10.1038/ncomms12334**.

29 H. Hu, X. Yang, X. Guo, K. Khaliji, S. R. Biswas, F. Javier García de Abajo, T. Low, Z. Sun and Q. Dai, Gas identification with graphene plasmons, *Phys. Rev. Appl.*, 2019, **10**, 1131, DOI: **10.1103/PhysRevApplied.13.011002**.

30 D. Rodrigo, O. Limaj, D. Janner, D. Etezadi, F. Javier García de Abajo, V. Pruneri and H. Altug, Mid-infrared plasmonic biosensing with graphene, *Science*, 2015, **349**, 165–168, DOI: **10.1126/science.aab2051**.

31 Y. Li, H. Yan, D. B. Farmer, X. Meng, W. Zhu, R. M. Osgood, T. Heinz and P. Avouris, Graphene Plasmon Enhanced Vibrational Sensing of Surface-Adsorbed Layers, *Nano Lett.*, 2014, **14**, 1573–1577, DOI: **10.1021/nl404824w**.

32 J. Nong, L. Tang, G. Lan, P. Luo, Z. Li, D. Huang, J. Shen and W. Wei, Combined Visible Plasmons of Ag Nanoparticles and Infrared Plasmons of Graphene Nanoribbons for High-Performance Surface-Enhanced Raman and Infrared Spectroscopies, *Small*, 2021, **17**, 2004640, DOI: **10.1002/smll.202004640**.

33 G. Dobrik, P. Nemes-Incze, B. Majerus, P. Süle, P. Vancsó, G. Piszter, M. Menyhárd, B. Kalas, P. Petrik and L. Henrard, Large-area nanoengineering of graphene corrugations for visible-frequency graphene plasmons, *Nat. Nanotechnol.*, 2022, **17**, 61–66, DOI: **10.1038/s41565-021-01007-x**.

34 A. Marini, I. Silveiro and F. Javier García de Abajo, Molecular sensing with tunable graphene plasmons, *ACS Photonics*, 2015, **2**, 876–882, DOI: **10.1021/acsphotonics.5b00067**.

35 Y. Kurman, N. Rivera, T. Christensen, S. Tsesses, M. Orenstein, M. Soljačić, J. D. Joannopoulos and I. Kaminer, Control of semiconductor emitter frequency by increasing polariton momenta, *Nat. Photonics*, 2018, **12**, 423–429, DOI: **10.1038/s41566-018-0176-6**.

36 S. Chakraborty, O. P. Marshall, T. G. Folland, Y. J. Kim, A. N. Grigorenko and K. S. Novoselov, Gain modulation by graphene plasmons in aperiodic lattice lasers, *Science*, 2016, **351**, 246–248, DOI: **10.1126/science.aad293**.

37 Q. Bao and K. Loh, Graphene photonics, plasmonics, and broadband optoelectronic devices, *ACS Nano*, 2012, **6**, 3677–3694, DOI: **10.1021/nn300989g**.

38 Q. Guo, C. Li, B. Deng, S. Yuan, F. Guinea and F. Xia, Infrared nanophotonics based on graphene plasmonics, *ACS Photonics*, 2017, **4**, 2989–2999, DOI: **10.1021/acsphotonics.7b00547**.

39 N. Bareza Jr., K. Gopalan, R. Alani, B. Paulillo and V. Pruneri, Mid-infrared Gas Sensing Using Graphene Plasmons Tuned by Reversible Chemical Doping, *ACS Photonics*, 2020, **7**, 879–884, DOI: **10.1021/acsphotonics.9b01714**.

40 Y. Li, N. An, Z. Lu, Y. Wang, B. Chang, T. Tan, X. Guo, X. Xu, J. He, H. Xia, Z. Wu, Y. Su, Y. Liu, Y. Rao, G. Soavi and B. Yao, Nonlinear co-generation of graphene plasmons for optoelectronic logic operations, *Nat. Commun.*, 2022, **13**, 3138, DOI: **10.1038/s41467-022-30901-8**.

41 J. Nong, L. Tang, G. Lan, P. Luo, Z. Li, D. Huang, J. Yi, H. Shi and W. Wei, Enhanced Graphene Plasmonic Mode Energy for Highly Sensitive Molecular Fingerprint Retrieval, *Laser Photonics Rev.*, 2021, **15**, 2000300, DOI: **10.1002/lpor.202000300**.

42 Z. Ma, K. Kikunaga, H. Wang, S. Sun, R. Amin, R. Maiti, M. H. Tahersima, H. Dalir, M. Miscuglio and V. J. Sorger, Compact Graphene Plasmonic Slot Photodetector on Silicon-on-Insulator with High Responsivity, *ACS Photonics*, 2020, **7**, 932–940, DOI: **10.1021/acsphotonics.9b01452**.

43 H. Yan, T. Low, W. Zhu, Y. Wu, M. Freitag, X. Li, F. Guinea, P. Avouris and F. Xia, Damping pathways of mid-infrared plasmons in graphene nanostructures, *Nat. Photonics*, 2013, **7**, 394–399, DOI: **10.1038/nphoton.2013.57**.

44 J. Chen, M. Badioli, P. Alonso-González, S. Thongrattanasiri, F. Huth, J. Osmond, M. Spasenović, A. Centeno, A. Pesquera, P. Godignon, A. Z. Elorza, N. Camara, F. Javier García de Abajo, R. Hillenbrand and F. Koppens, Optical nano-imaging of gate-tunable graphene plasmons, *Nature*, 2012, **487**, 77–81, DOI: **10.1038/nature11254**.

45 Z. Fei, A. Rodin, G. O. Andreev, W. Bao, A. McLeod, M. Wagner, L. Zhang, Z. Zhao, M. Thiemens, G. Dominguez, M. M. Fogler, A. H. Castro Neto, C. N. Lau, F. Keilmann and D. N. Basov, Gate-tuning of graphene plasmons revealed by infrared nano-imaging, *Nature*, 2012, **487**, 82–85, DOI: **10.1038/nature11253**.

46 X. Yang, F. Zhai, H. Hu, D. Hu, R. Liu, S. Zhang, M. Sun, Z. Sun, J. Chen and Q. Dai, Far–field spectroscopy and near–field optical imaging of coupled Plasmon–phonon polaritons in 2D van der Waals heterostructures, *Adv. Mater.*, 2016, **28**, 2931–2938, DOI: **10.1002/adma.201505765**.

47 V. W. Brar, M. S. Jang, M. Sherrott, S. Kim, J. Lopez, L. B. Kim, M. Choi and H. Atwater, Hybrid Surface-Phonon-Plasmon Polariton Modes in Graphene/Monolayer h-BN Heterostructures, *Nano Lett.*, 2014, **14**, 3876–3880, DOI: **10.1021/nl501096s**.

48 A. M. Dubrovkin, J. Tao, X. C. Yu, N. I. Zheludev and Q. J. Wang, The reduction of surface plasmon losses in quasi-suspended graphene, *Sci. Rep.*, 2015, **5**, 09837, DOI: **10.1038/srep09837**.

49 H. Hu, X. Guo, D. Hu, Z. Sun, X. Yang and Q. Dai, Flexible and electrically tunable plasmons in graphene–mica heterostructures, *Adv. Sci.*, 2018, **5**, 1800175, DOI: **10.1002/advs.201800175**.

50 Y. Qu, N. Chen, H. Teng, H. Hu, J. Sun, R. Yu, D. Hu, M. Xue, C. Li, B. Wu, J. Chen, Z. Sun, M. Liu, Y. Liu, F. Javier García de Abajo and Q. Dai, Tunable planar focusing based on hyperbolic phonon polaritons in α–MoO_3, *Adv. Mater.*, 2022, **34**, 2105590, DOI: **10.1002/adma.202105590**.

51 H. Hu, N. Chen, H. Teng, R. Yu, Y. Qu, J. Sun, M. Xue, D. Hu, B. Wu, C. Li, J. Chen, M. Liu, Z. Sun, Y. Liu, P. Li, S. Fan, F. Javier García de Abajo and Q. Dai, Doping-driven topological polaritons in graphene/α-MoO_3 heterostructures, *Nat. Nanotechnol.*, 2022, **17**, 940–946, DOI: **10.1038/s41565-022-01185-2**.

52 X. Yang, X. T. Kong, B. Bai, Z. Li, H. Hu, X. Qiu and Q. Dai, Substrate phonon–mediated plasmon hybridization in coplanar graphene nanostructures for broadband plasmonic circuits, *Small*, 2015, **11**, 591–596, DOI: **10.1002/smll.201400515**.

53 G. Wu, X. Tang, M. Meyyappan and K. W. Lai, Doping effects of surface functionalization on graphene with aromatic molecule and organic solvents, *Appl. Surf. Sci.*, 2017, **425**, 713–721, DOI: **10.1016/j.apsusc.2017.07.048**.

54 H. K. Christenson and N. Thomson, The nature of the air-cleaved mica surface, *Surf. Sci. Rep.*, 2016, **71**, 367–390, DOI: **10.1016/j.surfrep.2016.03.001**.

55 S. Goniszewski, M. Adabi, O. Shaforost, S. Hanham, L. Hao and N. Klein, Correlation of p-doping in CVD Graphene with Substrate Surface Charges, *Sci. Rep.*, 2016, **6**, 22858, DOI: **10.1038/srep22858**.

56 G. Redhammer, A. Beran, J. Schneider, G. Amthauer and W. Lottermoser, Spectroscopic and structural properties of synthetic micas on the annite-siderophyllite binary:

Synthesis, crystal structure refinement, Mossbauer, and infrared spectroscopy, *Am. Mineral.*, 2000, **85**, 449–465, DOI: **10.2138/am-2000-0406**.

57 V. Šontevska, G. Jovanovski, P. Makreski, A. Raškovska and B. Šoptrajanov, Minerals from Macedonia. XXI. Vibrational spectroscopy as identificational tool for some phyllosilicate minerals, *Acta Chim. Slov.*, 2008, **55**(4), 757–766.

58 H. Yan, T. Low, F. Guinea, F. Xia and P. Avouris, Tunable Phonon-Induced Transparency in Bilayer Graphene Nanoribbons, *Nano Lett.*, 2014, **14**, 4581–4586, DOI: **10.1021/nl501628x**.

59 C. H. Lui, L. Liu, K. F. Mak, G. W. Flynn and T. Heinz, Ultraflat graphene, *Nature*, 2009, **462**, 339–341, DOI: **10.1038/nature08569**.

60 X. Yang, Z. Sun, T. Low, H. Hu, X. Guo, F. Javier García de Abajo, P. Avouris and Q. Dai, Nanomaterial–based plasmon–enhanced infrared spectroscopy, *Adv. Mater.*, 2018, **30**, 1704896, DOI: **10.1002/adma.201704896**.

61 H. Teng, N. Chen, H. Hu, F. Javier García de Abajo and Q. Dai, Steering and cloaking of hyperbolic polaritons at deep-subwavelength scales, *Nat. Commun.*, 2024, **15**, 4463, DOI: **10.1038/s41467-024-48318-w**.